Loan 1036 "Rift Volcanism: Past, Present and Future [RiftVolc]"

Abstract

As part of a survey of the resistivity structure of the central main Ethiopian rift we used the GEF TEM and solar panels in 2016, and just solar panels in 2017. Solar panels were used to power magnetotelluric (MT) systems borrowed from Dublin, Ireland. The equipment performed as expected but the MT data quality was only average owing to significant civil unrest at the times of our surveys. Nevertheless our 2016 data were sufficient to publish a 2D cross-rift profile model, and we are in the process of preparing a manuscript on a 3D model of a broader area; the latter was presented at the 2020 virtual EGU meeting. The western flank of the rift is associated with high conductivities, interpreted as abundant melt, whilst the restive Aluto volcano is underlain by a prominent resistor. Our 3D model has ubiquitous high conductivities in the lower crust, away from the Wonji fault belt to the south-east. The extent and location of this feature corresponds well with a low shear wave speed feature obtained from ambient noise tomography.

Background

The loan consisted of 8 regulated solar panels and a complete Geonics TEM system, consisting of a TEM 47 transmitter and PROTEM receiver plus various batteries, cables, coils and a laptop with dongle (in 2016) and 8 regulated solar panels (in 2017). Figure 1 shows our MT sites from both seasons, comprising 57 broadband and 12 long period sites.

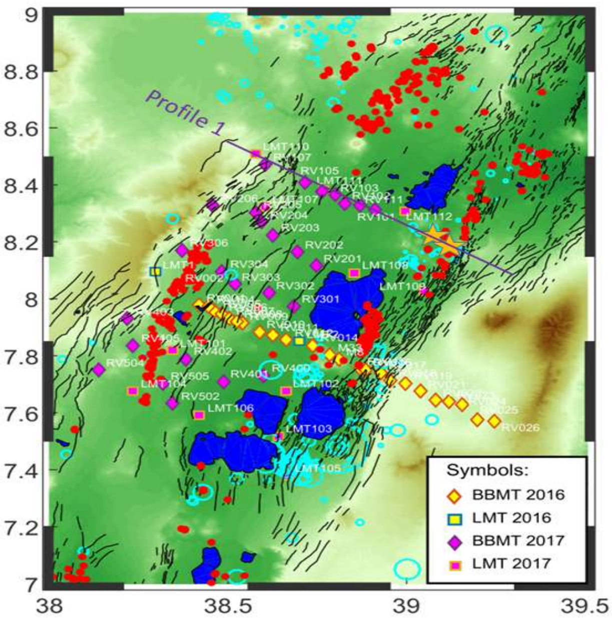

Figure 1. Broadband (BBMT) and long period (LMT) sites collected on this loan. Red dots are volcanic vents, cyan circles are seismicity recorded during the EAGLE project in 2002-4 (circle size indicates magnitude), and the black lines are faults. The two stars at the south-east end of Profile 1 are broadband sites collected over a geothermal project by Reykjavik Geothermal.

Survey procedure

Each MT system was attached to 2 solar panels (broadband sites) or 1 solar panel (long period sites) for the full recording time. After some experimentation, the TEM system was deployed with a 100 m x 100 m square source loop, with effective receiver loop size of 31.4 m^2, and integration times from 0.25 to 120 s. TEM data were collected at all sites from the 2016 campaign (yellow diamonds in Figure 1).

Data quality

TEM data were of good quality (see Figure 2). MT data quality was variable, owing primarily to significant civil unrest at the times of our surveys. People interfered with our equipment and threatened our guards. Some sites had to be brought in early, compromising the long period data we hoped to collect. Other places where we would have liked to install sites were not deemed safe enough or could not have been accessed safely, or road closures meant we were unable to travel to and from them. These difficulties also reduced the number of sites we occupied. Since we were intending to produce a 3D model from data from season 2, where galvanic distortion is less of an issue, and because of the fieldwork challenges anticipated (and realised), we decided not to collect TEM data in 2017.

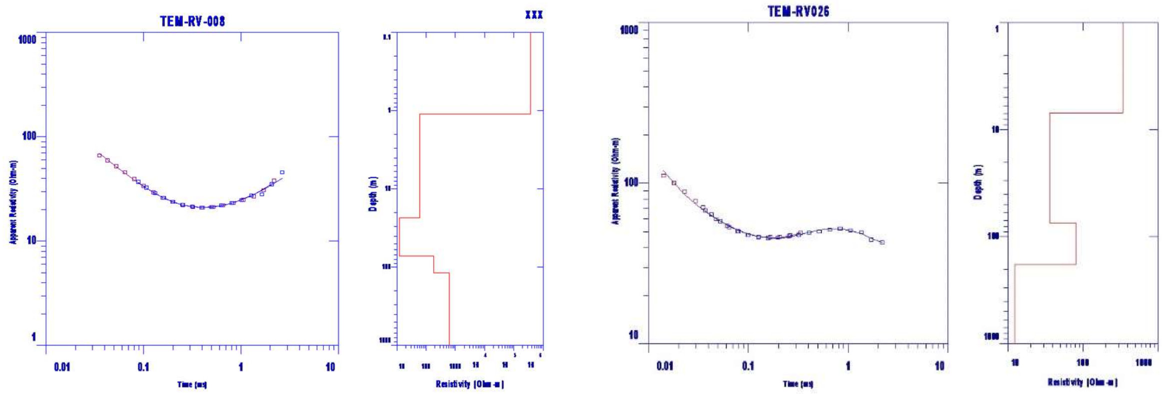

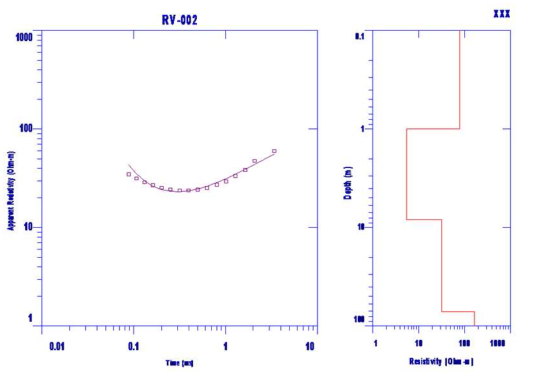

Figure 2. Processed TEM data (left hand panel of each plot) shown as circles and 1D resistivity model (right hand panel) from 3 TEM sites. Data predicted by the model on the right are shown as a continuous line. Site number indicated at top of left hand panel.

Sample off-diagonal MT impedance tensor elements, and tipper components for long period sites, are shown in Figure 3.

a)

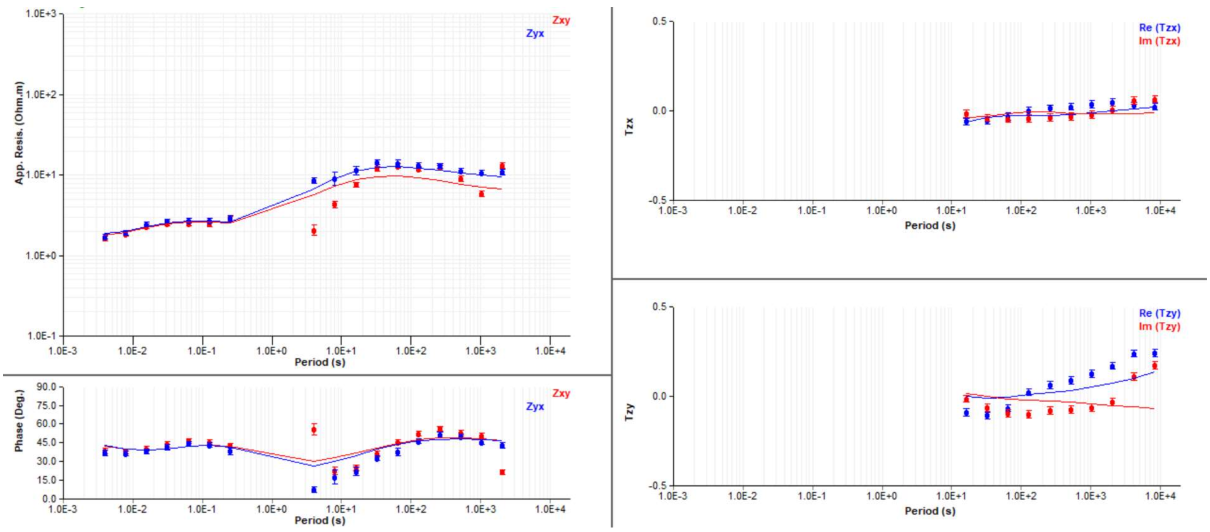

b)

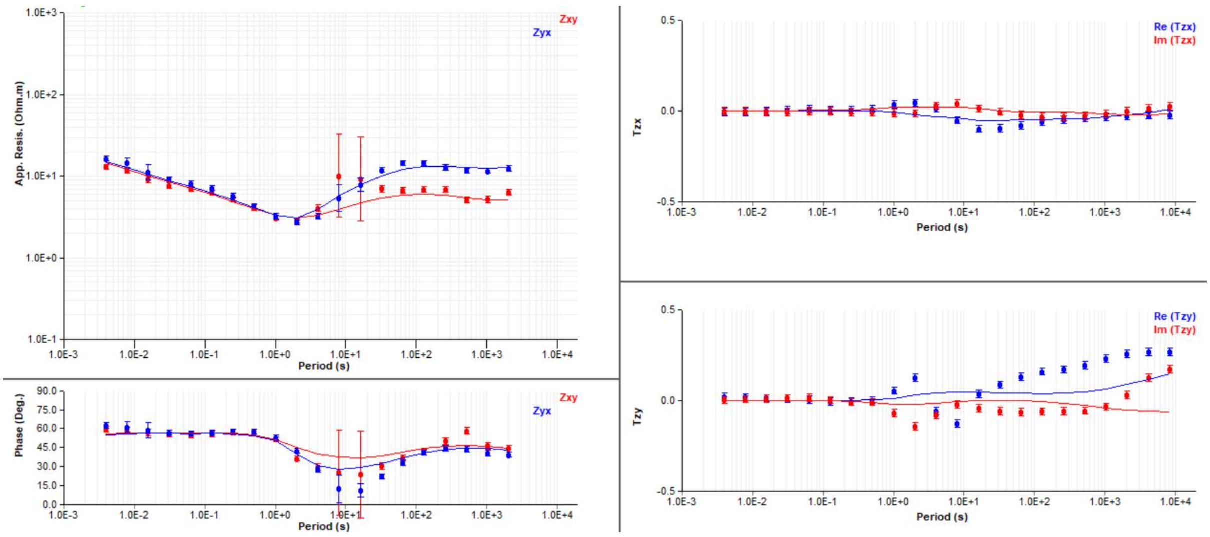

c)

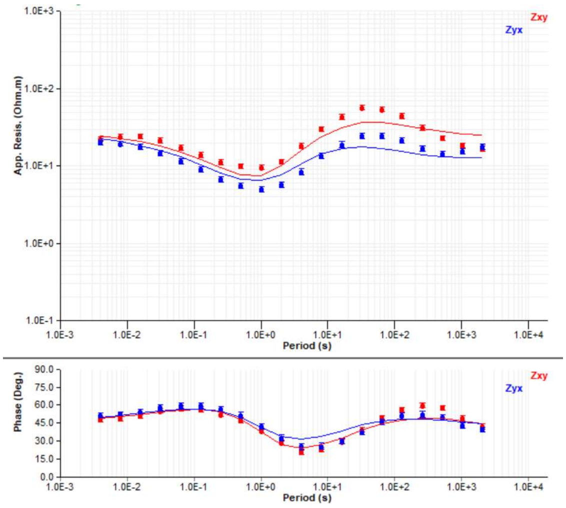

d)

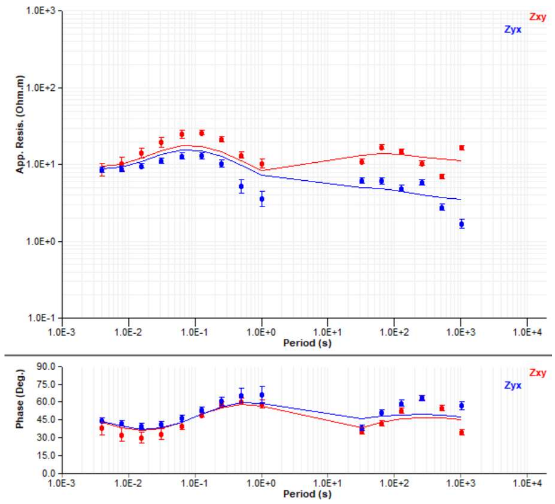

Figure 3. Off-diagonal components of the impedance tensor, **Z**, plotted as apparent resistivity and phase as a function of period, with xy component in red and yx component in blue; for the long period sites, tipper vectors, **T**, are also plotted, with real part in blue and imaginary part in red, top panel showing zx component and bottom part zy component. Solid lines are the predictions of the model shown in figure 6. a) site LMT106, b) site LMT103, c) site BB402, d) site BB205.

Processing and modelling

TEM data were processed to provide apparent resistivity as a function of time (left hand panels of figure 2) and then inverted for 1D layered models of resistivity as a function of depth (right hand panels of figure 2). The data predicted by the models are shown as continuous lines on the data plots.

MT data were robustly processed using remote referencing (based on the codes of Egbert (1997) and Smirnov (2003) for BBMT and LMT respectively) to calculate the impedance tensor elements as a function of period. The fluxgate magnetometers in the LMT systems measured all three magnetic field components, enabling tipper vectors also to be estimated.

For data collected in 2016, phase tensors (figure 4) and other analyses indicated that they were broadly consistent with a 2D interpretation. Strike analysis (Zhang et al., 1987) did not indicate any dominant geoelectrical strike direction, so we chose it to be trend of the rift, 28°N. The determinant average (DET) is invariant to strike angle and should be less noisy than the individual TE and TM components. We applied regularised inversion to the DET apparent resistivity and phase, and also the TE and TM modes separately and together, using the code of Kalscheuer et al. (2008). A fine model discretization between adjacent stations along the profile allows the inversion to introduce small near-surface heterogeneities, compensating for static shift (rather than correcting the data prior to inversion). The model and root-mean-square misfit did not vary much as the error floor varied between 10% and 90%. Nor did they change significantly with the starting homogeneous half-space resistivity value. Figure 5 shows our preferred model, from inversion of the DET data; others are shown in the supplementary material of Hübert et al. (2018). The robustness of the main features was established by sensitivity tests. Subsequently, Dambley et al. (2020) obtained a similar result with 3D inversion of the data (including additional sites over the Aluto volcano) using a 3D code (Grayver, 2015).

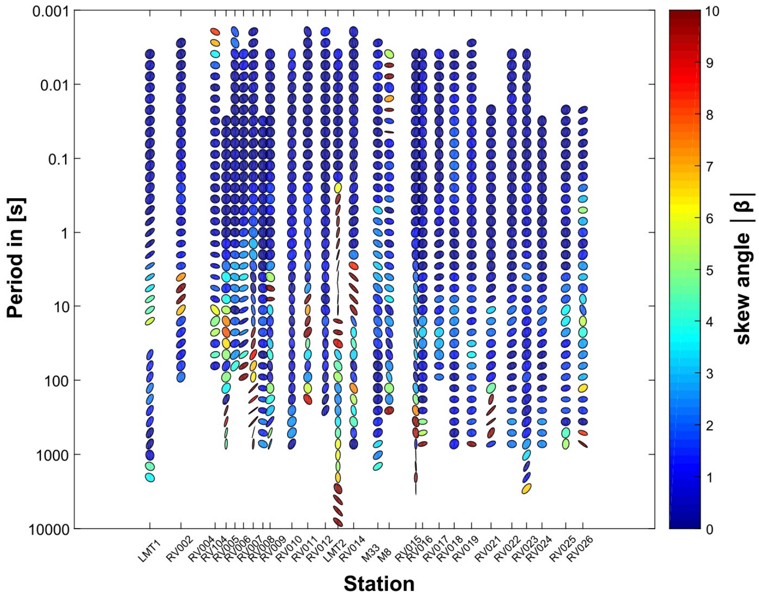

Figure 4. Phase tensors as a function of period for sites along the 2016 cross-rift profile (yellow diamonds in Figure 1), from north-west to south-east. Roughly circular shape and low β angle (colour fill) suggest consistency with a 2D Earth. From Hübert et al. (2018).

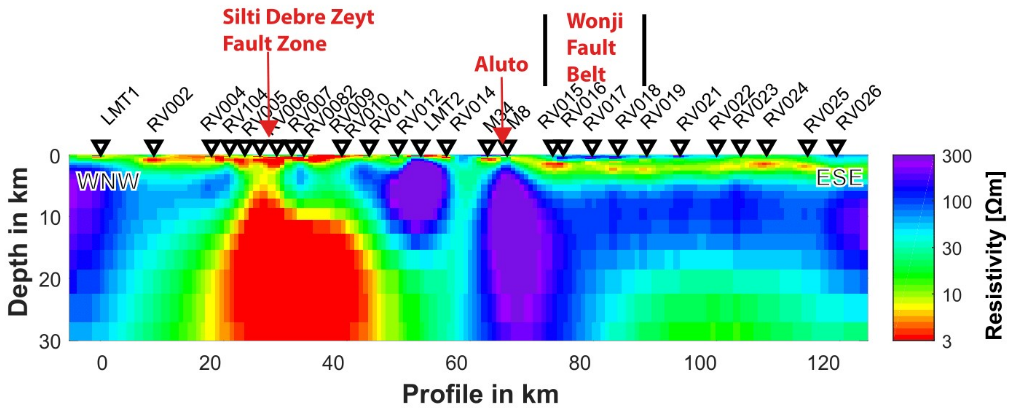

Figure 5. 2D model along 2016 profile. The Silte Debre Zeyt fault zone is close to the northern escarpment of the rift, Aluto is a volcano within a Quaternary magmatic segment in the rift, and the Wonji fault belt marks the southern extent of the rift. (Hübert et al., 2018).

Impedance tensors and, where available, tippers, from all sites collected in this project, and two provided by Reykjavik Geothermal over one of their geothermal concessions (see figure 1), were inverted for a 3D model. Depth slices through it are shown in figure 6. Data predictions are the continuous lines on figure 3.

Interpretation/preliminary findings

Samrock et al. (2015) undertook a local MT survey of Aluto volcano. They inferred a resistor beneath the volcano, in contrast to high conductivity beneath other Ethiopian volcanoes. The result was even more surprising as the volcano is actively deforming and degassing (Hutchison et al., 2016), so a magma reservoir, that would normally be conductive, is expected. Subsequently, Wilks et al. (2017) inferred that the magma reservoir is bubbly, meaning the melt will be poorly connected and hence the bulk resistivity will be high. Our survey confirms the high resistivity beneath Aluto, and that Samrock et al.'s (2015) result is not because of the limited aperture of their array. Samrock et al (2015) also inferred the existence of a good conductor to the north-west from the orientation and magnitude of the long period induction vectors, again confirmed in our survey. Our induction vectors and 3D model imply this is an elongated feature along the Silte Debre Zeyt fault zone (SDZF, figure 7). However, challenges remain in the interpretation. Iddon et al.'s (2019) melt inclusion data indicate high water content for Aluto melt, but low water content for SDZF melt, suggesting low and high resistivity respectively, in contrast to observations.

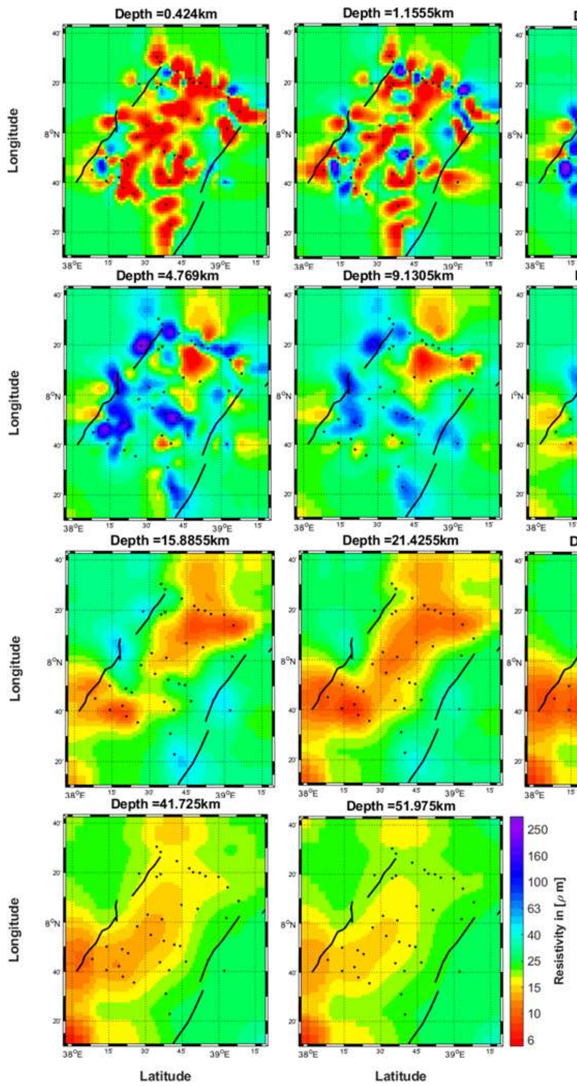

Figure 6. Depth slices through the 3D model. Major border faults are shown as black lines, and sites as black dots.

The extent of our lower crustal conductor agrees reasonably well with the low shear velocity region in Chambers et al.'s (2020) ambient noise tomography model (figure 8). However, neither MT nor ambient noise tomography has the resolution to determine whether melt is widespread, as in the models, or in laterally constrained regions. Geochemical signatures are different for volcanic products on the flanks of and in the rift, but the differentiation could be during ascent from a common source.

We have also begun an analysis of electrical anisotropy, where the direction is given by the geoelectrical strike direction (with 90° ambiguity) and the amount by the maximum difference between the off-diagonal phases when the data are rotated into coordinates defined by the geoelectrical strike direction (e.g. Padilha et al., 2006). It is period dependent, but we seek period bands in which the geoelectrical strike direction is constant. The analysis is predicated on the data being consistent with a 2D Earth; this is one of the major limitations. Preliminary results are given in figure 9. We will undertake a comparison with seismic anisotropy, provided by several separate studies.

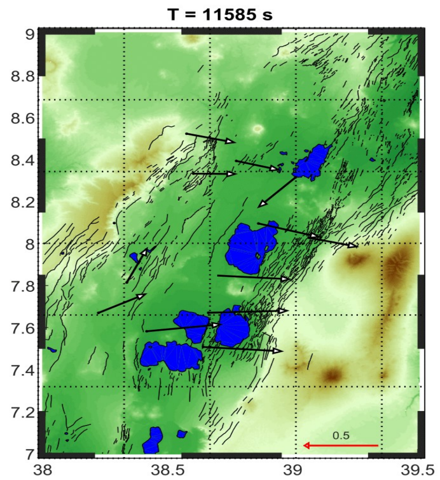

Figure 7. Real components of the induction (tipper) vector at a period of 11585 s. In the Weise convention used here, the vectors point away from conductors.

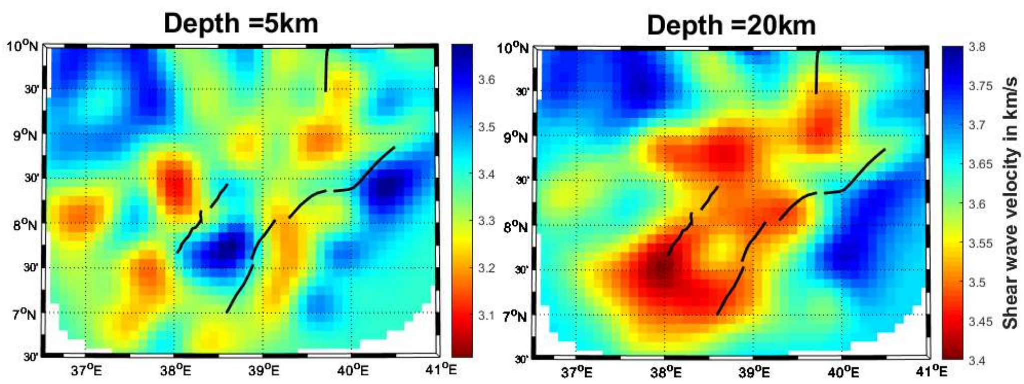

Figure 8. Depth slices through the shear wave velocity model of Chambers et al. (2020).

Conclusions and recommendations

Despite somewhat disappointing data quality, we have produced 2D and 3D resistivity models of the field area, resolving structure in the lower crust and uppermost mantle of the rift for the first time. We have begun an interpretation of them in conjunction with other geophysical and geochemical data. There is a good conductor associated with the SDZF, and the lower crust is electrically conductive, except in the region on the Wonji fault belt.

References

Chambers, E. L., et al. (2019). Using ambient noise to image the northern East African Rift. Geochem., Geophys., Geosyst., 20, 2091–2109. DOI: 10.1029/2018GC008129

Dambley, M. L. T., Samrock, F., Grayver, A. and Saar, M. O. (2020). Combined Multi-Scale Inversion of Regional and Local Magnetotelluric Data from the Main Ethiopian Rift. AGU Fall Meeting (https://agu2020fallmeeting-agu.ipostersessions.com/Default.aspx?s=51-7D-7E-E8-EA-2B-75-5E-93-C1-47-0E-DF-AC-05-01&pdfprint=true&guestvie%E2%80%A6)

Egbert, G. D. (1997). Robust multiple-station magnetotelluric data processing. *Geophys. J. Int.*, **130**, 475–496

Grayver, A. V. (2015). Parallel three-dimensional magnetotelluric inversion using adaptive finite-element method. Part I: Theory and synthetic study. *Geophys. J. Int.,* **202**, 584–603

Hübert, J., Whaler, K., Fisseha, S. (2018). The electrical structure of the Central Main Ethiopian Rift as imaged by magnetotellurics: Implications for magma storage and pathways. J. Geophys. Res., 123, 6019-6032. DOI: 10.1029/2017JB015160

Hutchison, W., et al. (2016) Causes of unrest at silicic calderas in the East African Rift: New constraints from InSAR and soil-gas chemistry at Aluto volcano, Ethiopia, *Geochem. Geophys. Geosyst.*, **17**, 3008–3030, doi:10.1002/2016GC006395

Iddon F., et al. (2019). Mixing and crystal scavenging in the Main Ethiopian Rift revealed by trace element systematics in feldspars and glasses. Geochem., Geophys., Geosyst., 20, 230-59, DOI: 10.1029/2018GC007836

Kalscheuer, T., Pedersen, L. B., & Siripunvaraporn, W. (2008). Radiomagnetotelluric two-dimensional forward and inverse modelling accounting for displacement currents. *Geophysical Journal International*, *175*(2), 486–514.

Padilha, A., Vitorello, Í., Pádua, M., Bologna, M. (2006). Lithospheric and sublithospheric anisotropy beneath central-southeastern Brazil constrained by long period magnetotelluric data, *Phys. Earth Planet. In.*, **158**, 190-209

Samrock, F., et al. (2015). 3D analysis and interpretation of Magnetotelluric data from the Aluto-Langano geothermal field, Ethiopia. *Geophys. J. Int.*, **202**, 1923-1948

Smirnov, M. Y. (2003). Magnetotelluric data processing with a robust statistical procedure having a high breakdown point. *Geophys. J. Int.*, **152**, 1–7

Wilks, M., et al. (2017). Seismicity associated with magmatism, faulting and hydrothermal circulation at Aluto Volcano, Main Ethiopian Rift, *J. Volcanol. Geotherm. Res.*, **340**, 52-67

Zhang, P., Roberts, R. G., & Pedersen, L. B. (1987). Magnetotelluric strike rules. *Geophysics*, **52**, 267–278

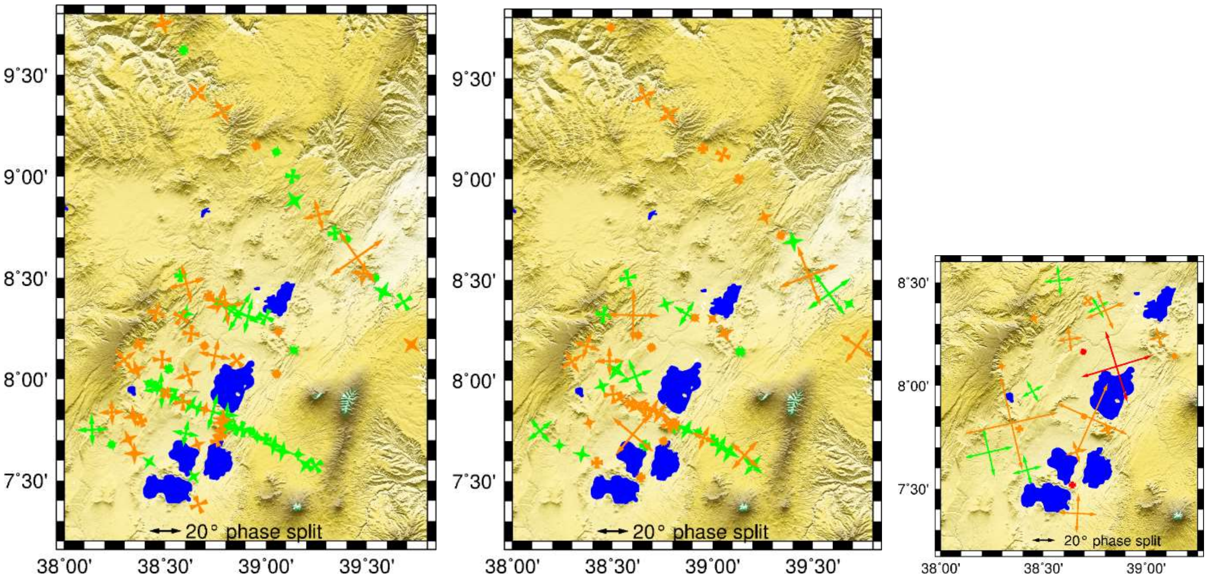

Figure 9. Electrical anisotropy in the main Ethiopian rift for the upper-mid crust (left), lower crust (middle) and mantle (right). Arrows show the 90° ambiguity; their length indicates the phase split. Results are colour coded according to their consistency with a 2D Earth, indicating their reliability. Green results are the most reliable, amber are fair, and red, shown only for the mantle, are poor. Legacy data from the NERC funded and GEF supported EAGLE project are included.

Instrument deployment details

Station locations. TEM data were collected at those marked with an asterisk.

LMT101	7.8178	38.34367
LMT102	7.67729	38.66032
LMT103	7.51817	38.64013
LMT104	7.67665	38.2337
LMT105	7.37978	38.66531
LMT106	7.59117	38.42101
LMT107	8.32363	38.60204
LMT108	8.09221	38.85454
LMT109	8.02557	39.05119
LMT110	8.50908	38.5758
LMT111	8.38268	38.76871
LMT112	8.30596	38.99826
M12	7.76725	38.80809
M33	7.803	38.7859
M34	7.73277	38.77684
M8	7.78782	38.81018
RV001	8.09405	38.29553
RV002*	8.04693	38.35744
RV003*	7.99922	38.37843
RV004	7.9778	38.41807
RV005*	7.95695	38.46278
RV006*	7.94512	38.48059

RV019	7.70364	38.99883
RV021	7.67347	39.0384
RV022	7.64433	39.08054
RV023	7.637	39.11924
RV024	7.62789	39.15842
RV025*	7.57703	39.19806
RV026*	7.57207	39.24382
RV027	7.54254	39.25876
RV101	8.31096	38.91072
RV102	8.33608	38.82557
RV103	8.36374	38.79972
RV104	8.37879	38.76397
RV105*	8.40996	38.7165
RV107	8.471	38.60445
RV111	8.3302	38.86879
RV201	8.11546	38.74578
RV202	8.16394	38.69384
RV203	8.22411	38.62699
RV204	8.26822	38.5954
RV205	8.30485	38.57713
RV206	8.32694	38.4548
RV301	7.97401	38.68465

RV007*	7.93102	38.5013
RV008*	7.9205	38.52265
RV009*	7.91286	38.53944
RV010*	7.88499	38.58646
RV0104	7.97195	38.44636
RV011*	7.87402	38.62536
RV012*	7.85469	38.66508
RV013*	7.85005	38.69753
RV014*	7.83866	38.73546
RV015	7.75542	38.86765
RV016	7.75186	38.88465
RV017	7.74208	38.92735
RV018	7.71411	38.95479

RV302	8.02008	38.6132
RV303	8.05044	38.51675
RV304	8.09609	38.48425
RV306	8.17156	38.37065
RV400	7.73106	38.60051
RV401	7.71058	38.48502
RV402	7.79015	38.38233
RV403	7.92844	38.21864
RV405	7.8361	38.23532
RV502	7.63248	38.34647
RV504	7.74983	38.13653
RV505	7.7033	38.3177

Archived data

Data are almost ready to be submitted to NGDC. Accompanying metadata includes far greater detail of deployment than given above, e.g. sensor numbers, electric line lengths, and processing details.

Peer reviewed publications

Hübert, J., Whaler, K., Fisseha, S. (2018). The electrical structure of the Central Main Ethiopian Rift as imaged by magnetotellurics: Implications for magma storage and pathways. J. Geophys. Res., 123, 6019-6032. DOI: 10.1029/2017JB015160

Conference presentations

Hübert, J., Whaler, K., Fisseha, S. From 'shoulder to shoulder' – A cross-rift Magnetotelluric Transect through Aluto volcano, Ethiopia, 23rd Electromagnetic induction workshop, Chiang Mai, Thailand, 2016

Hübert, J., Whaler, K., Fisseha, S. Evidence for off-axis magma pathways in the Central Main Ethiopian Rift as imaged by Magnetotellurics, TSG-VMGS-BGA Joint assembly, Liverpool, UK, 2017

Hübert, J., Whaler, K. and S. Fisseha, S. Magnetotelluric imaging of the Central Main Ethiopian Rift - Implications for magma pathways and storage, IAGA Scientific Assembly, Cape Town, South Africa, 2017

Hübert, J., Whaler, K.; Fisseha, S. and Hogg, C. Imaging an off-axis volcanic field in the Main Ethiopian Rift using 3-D magnetotellurics, AGU Fall meeting 2017

Hübert, J., Whaler, K.; Fisseha, S. and Hogg, C. Bi-modal Magma Storage across the Main Ethiopian Rift Zone as imaged by 3-D Magnetotellurics, 24th EM Induction Workshop, Helsingør, Denmark, 2018

Iddon, F., Edmonds, M.; Hübert, J. and Whaler, K. Missing Melts: Reconciling geochemical and geophysical observations of magma storage across the Main Ethiopian Rift, RiftVolc Conference 'Magmatic and Volcanic Processes in Continental Rifts', Hawassa, Ethiopia, 2019

Hübert, J., Whaler, K.; Fisseha, S., Iddon, F. and Hogg, C. Bi-modal Magma Storage across the Main Ethiopian Rift Zone as imaged by 3-D Magnetotellurics, RiftVolc Conference 'Magmatic and Volcanic Processes in Continental Rifts', Hawassa, Ethiopia, 2019

K A Whaler, J O S Hammond, D Keir, J Hübert, S Fisseha, Electrical and Seismic Anisotropy in the Main Ethiopian Rift, Abstract, RiftVolc Conference 'Magmatic and volcanic processes in continental rifts', Hawassa, Ethiopia, 2019

Hübert, J., Whaler, K., Fisseha, S., Iddon, F. and Hogg, C. Imaging deep magmatic processes in an active continental rift zone using 3-D Magnetotellurics, IUGG General Assembly Montreal, Canada, 2019 (Invited)

K A Whaler, J O S Hammond, D Keir, J Hübert, S Fisseha, Electrical and Seismic Anisotropy in the Main Ethiopian Rift, IUGG General Assembly, Montreal, Canada, 2019

Hübert, J., Whaler, K., Fisseha, S., Iddon, F. and Hogg, C. Imaging magma storage in the Main Ethiopian Rift with 3-D Magnetotellurics, EGU General Assembly, 2020